JACS
JOURNAL OF THE AMERICAN CHEMICAL SOCIETY
Article
pubs.acs.org/JACS

General Synthetic Strategy for Hollow Hybrid Microspheres through a Progressive Inward Crystallization Process

Li-Ping Yang,[†,‡] Xi-Jie Lin,[†,§] Xing Zhang,[†,‡] Wei Zhang,[†,‡] An-Min Cao,*[,†,‡] and Li-Jun Wan*[,†,‡]

[†]Key Laboratory of Molecular Nanostructure and Nanotechnology and Beijing National Laboratory for Molecular Sciences, Institute of Chemistry, Chinese Academy of Sciences, Beijing 100190, People's Republic of China

[‡]University of Chinese Academy of Sciences, Beijing 100049, People's Republic of China

[§]State Key Laboratory of Fine Chemicals, Dalian University of Technology, Dalian 116024, People's Republic of China

Supporting Information

ABSTRACT: Hollow hybrid microspheres have found great potential in different areas, such as drug delivery, nanoreactors, photonics, and lithium-ion batteries. Here, we report a simple and scalable approach to construct high-quality hollow hybrid microspheres through a previously unexplored growth mechanism. Starting from uniform solid microspheres with low crystallinity, we identified that a hollowing process can happen through the progressive inward crystallization process initiated on the particle surface: the gradual encroachment of the crystallization frontline toward the core leads to the depletion of the center and forms the central cavity. We showed that such a synthetic platform was versatile and can be applicable for a large variety of materials. By using the production of $Li_4Ti_5O_{12}$–carbon hollow hybrid microspheres as an example, we demonstrated that high-performance anode materials could be achieved through synthesis and structure control. We expect that our findings offer new perspectives in different areas ranging from materials chemistry, energy storage devices, catalysis, to drug delivery.

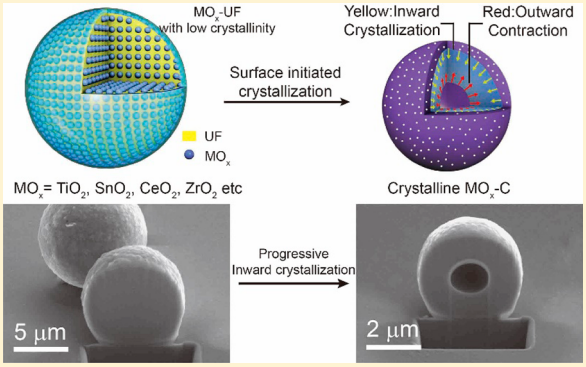

INTRODUCTION

Due to their unique structural features, hollow hybrid microspheres (HHMs) have attracted considerable attention in a wide range of applications, including lithium-ion batteries (LIBs), catalysis, drug delivery, photonics, and chemical sensors.[1−3] By controlling the shape and composition of HHMs, it becomes possible to endow HHMs with interesting properties and specific functions for designated purposes.[4−7] Typically, the well-defined interior cavity has been demonstrated as an ideal cage for encapsulation and release of functional materials, showing promising potential as a platform for drug delivery.[8,9] Meanwhile, the hollow space could function as an effective buffer zone to alleviate the mechanical stress and volume change. It has been widely reported that HHMs could act as a good mechanical buffer and electrolyte reservoir in LIBs, which is of great importance to ensure the mechanical integrity and structural stability of electrodes during continuous charge/discharge processes.

To unlock the potential of HHMs, numerous efforts have been exerted to identify suitable synthetic protocols so that model HHM systems can be fabricated in a controllable and repeatable way. Recent decades have witnessed the fast development of template-based synthesis by using either hard templates, typically solid powders such as SiO_2 particles,[10−13] or soft ones including micelles formed by surfactants.[13,14] Recent achievements show that even more complicated HHMs with multiple shells could be prepared by controlling distribution and interaction of the reactants inside the templates.[15−18] The template approach shows the capability of providing a straightforward way to create hollow structures. Unfortunately, it is usually time-consuming with tedious operating procedures, and it can only produce reduced quantity and quality of the applications. Scientists have been searching for template-free methods in light of their simplicity and potential for scale-up. Recent progress confirms that it is possible to create a central cavity through a spontaneous growth process with no need for the pre-existing templates.[19−21] Different formation mechanisms such as Kirkendall effect and/or the Ostwald ripening have been proposed as the possible driving forces for the hollowing process. However, the reported synthetic protocols usually work for independent HHM formation. It is in high demand to develop a versatile synthetic platform that not only is effective for a large variety of materials but also has key evidence in support of the growth mechanism. It is of equal importance that these syntheses could be convenient, low-cost, environmentally benign, and suitable for large-scale production.

For different HHMs, we have special interest in metal oxides due to their wide applications in different fields such as

Received: January 22, 2016
Published: April 20, 2016

DOI: 10.1021/jacs.6b00773
J. Am. Chem. Soc. 2016, 138, 5916−5922

catalysis, ceramics, and LIBs.[1,2] Typically, the spinel lithium titanium oxide of $Li_4Ti_5O_{12}$ (LTO) has been considered as a promising anode material in LIBs due to its extraordinary chemical and electrochemical stability, which is highly favorable for its application in electrical vehicles and energy storage devices.[22,23] However, the application of LTO is plagued by its extremely low electrical conductivity.[24,25] It has become an indispensable step for a suitable nanostructuring of LTO to alleviate its sluggish electrode kinetics. Different approaches, such as surface modification by conductive additives[26,27] and hollow structures by templating strategies,[10] turn out to be successful for improving battery performance in LIBs. As far as the kinetics problem in LIBs is concerned, it is highly desirable that metal oxides including LTO be engineered into favorable structures, for example, HHMs with hybrid composition composed by LTO embedded in an electronically conducting matrix.

In this paper, we report our progress on the synthesis of uniform HHMs for a large variety of metal oxides (MO_x), which include but are not limited to TiO_2, ZrO_2, CeO_2, and SnO_2. Hybrid materials such as MO_x–C and $M_xM'_{1-x}O$ could be conveniently produced in a large quantity through a template-free process. We demonstrate that the hollow interior is spontaneously induced by an interesting progressive inward crystallization process: particles first crystallize on the surface, and then the crystallization gradually proceeds inward, leading to the depletion of the core and simultaneous formation of a cavity. Using LTO as an example, we show that such a synthetic protocol could be very useful for production of promising anode materials. The prepared LTO–C HHMs are uniform hollow microspheres enclosed by a nanocomposite wall, in which conductive carbon is well-dispersed inside the LTO matrix. Our preliminary results show that LTO–C HHMs illustrate much improved battery performance with regard to the cyclability and rate capability of the anode material.

EXPERIMENTAL SECTION

Synthesis of TiO_2 Sol. Tetrabutyl titanate (TBOT, 35 mmol) was added into 60 mL of deionized water. The solution was stirred for 30 min at 60 °C, and a clear sol–gel was formed and stored for further use.

Synthesis of TiO_2–UF Microspheres. The final morphology of product is sensitive to the amount of TiO_2 sol used for the PICA process. To ensure the HHM formation, we used 5 mmol TiO_2 sol and dispersed it into 40 mL of deionized water. Next, 33 mmol urea was added, and the pH was adjusted to around 1.5 with concentrated hydrochloric acid. Then, 4 mL of formaldehyde (37 wt %) was added to start the reaction. The white precipitate was collected through centrifugation–rinse cycles and dried at 80 °C overnight for further characterization.

Synthesis of TiO_2–C HHMs. The white TiO_2–UF powder was transferred into a tube furnace that was heated to 700 °C at 1 °C/min in an inert atmosphere. TiO_2–C HHMs formed as a dark powder.

Synthesis of LTO–C HHMs. TiO_2–UF microspheres and a lithium source (lithium carbonate) were mixed with a Li/Ti mole ratio of 1:1. The mixture was transferred into a tube furnace and calcined at 800 °C for 12 h in an inert atmosphere to prepare LTO-C HHMs.

Synthesis of HHMs for Different Metal Oxides. See the Supporting Information Table S1 for details of the synthesis of different MO_x HHMs, including SnO_2, CeO_2, and ZrO_2 and their composites, as well.

Material Characterization. Field emission scanning electron microscopy (FESEM) images and energy-dispersive X-ray (EDX) analysis were acquired on a JEOL JSM-6701F microscope. The transmission electron microscopy (TEM) and high-resolution transmission electron microscopy (HRTEM) images were recorded on a JEOL-2100F microscope. EDX analysis also was acquired on a JEOL-2100F microscope. The SEM images and TEM specimen prepared by the focused ion beam (FIB) technique were collected on a Helios NanoLab 600i. X-ray diffraction (XRD) patterns were collected on a Rigaku D.MAX-2500 with Cu Kα radiation (λ = 1.5406 Å). Thermogravimetric analysis (TGA) was carried out with a SII WXSTAR6000-TGA6300 over the range of 20–800 °C in air or N_2 flow at a heating rate of 10 °C/min. The tap density was measured by a JZ-7 tap densitometer.

Electrochemical Measurements. Electrochemical measurements were tested with CR2032 coin cells at room temperature for half-cell and full-cell configurations. The electrode consists of 80 wt % active material, that is, $LiMn_{1.5}Ni_{0.5}O_4$ and LTO, respectively, 10 wt % Super-P, and 10 wt % poly(vinylidene fluoride) (PVDF, Aldrich) binder in *N*-methyl pyrrolidone (NMP, Aldrich). The slurry was stirred and cast onto Al or Cu foil (99.9%, Goodfellow). The electrodes were cut into circular electrodes of 0.64 cm^2 area, and the cathode and anode electrode density were 2.65 and 3.13 mg/cm^2, respectively. Pure lithium foil was used as the counter electrode for the half-cell. The electrolyte was composed of 1.0 M $LiPF_6$ in ethylene carbonate (EC)/diethyl carbonate (DEC). The galvanostatic charge/discharge tests were performed on a LAND CT2001A battery test system with a cutoff voltage window of 1.0–3.0 V vs Li^+/Li for half-cell and 1.5–3.4 V for full-cell. Electrochemical impedance spectral (EIS) measurements were acquired on an Autolab PGSTAT 302N electrochemical workstation over the frequency range from 100 kHz to 100 mHz at room temperature.

RESULTS AND DISCUSSION

For a typical synthesis of HHMs, it starts with the preparation of inorganic–organic microspheres as the precursor. A polymerization-induced colloid aggregation (PICA) process is adopted to form uniform microspheres with a narrow size distribution (Scheme 1). Use of this PICA process lies in not only its capability of morphology control but also its simplicity to implement as an industrially scalable operation based on cheap and environmentally benign source materials. First, metal oxide sol is prepared by using a typical sol–gel process (step 1). These MO_x sols usually either are amorphous or show a very low crystallinity. A PICA process is then enforced through the in situ polymerization of urea–formaldehyde (UF) in the MO_x sol (step 2), resulting in the aggregation of MO_x colloids into the UF resin for the formation of MO_x–UF microspheres. Heat

Scheme 1. Schematic Illustration for the Formation Process of Hollow Hybrid Microspheres[a]

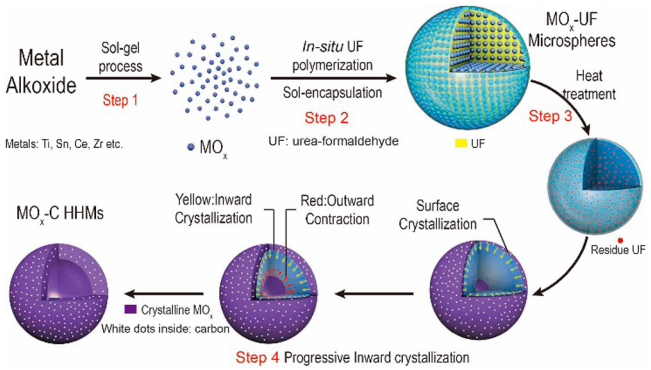

[a]Step 1: MO_x sol formation through a sol–gel process. Step 2: In situ polymerization process for inorganic–organic microspheres with sol encapsulated inside the UF matrix. Step 3: Heating-induced particle contraction. Step 4: HHM formation through progressive inward crystallization.

DOI: 10.1021/jacs.6b00773
J. Am. Chem. Soc. 2016, 138, 5916–5922

treatment can quickly condense these microspheres into smaller size due to the loss of a large amount of UF species (step 3). The surface and core thereafter change in a correlative way as a result of the progressive crystallization (step 4): Crystallization starts on the surface and then gradually proceeds inward. Meanwhile, the center cracks, and the amorphous interior contracts outward. These two trends, or the inward crystallization and the outward contraction, happen simultaneously and finally form highly crystalline microspheres with a characteristic hollow center. If the heating happens in an inert atmosphere, a high-temperature treatment will turn the residue UF into conductive carbon, which will be well-dispersed inside the MO_x matrix to form the MO_x–C HHM composite. Otherwise, heating in air will produce the MO_x HHMs only.

With the preparation of TiO_2–C HHMs as an example, a TiO_2 sol was first prepared to form tiny TiO_2 colloids with a size of around 8 nm (for methods of the experimental details and the characterizations on TiO_2 sol, see the Supporting Information, Figure S1). To start a typical PICA process, fresh TiO_2 sol is introduced into the aqueous solution of urea and formaldehyde, and then UF polymerization under acid conditions would immediately assemble tiny colloids into a large monolith, forming a hybrid inorganic–organic product with TiO_2 colloids dispersed inside the UF resin. Figure 1a

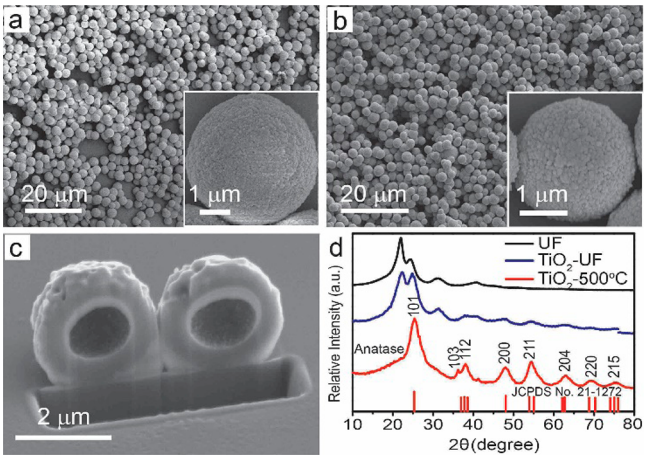

Figure 1. (a–c) SEM images and (d) XRD patterns of TiO_2–UF microspheres and TiO_2–C HHMs: (a) TiO_2–UF, (b) TiO_2–C HHMs, (c) FIB-prepared cross section of TiO_2–C HHMs, and (d) XRD patterns of UF, TiO_2–UF, and TiO_2–C HHMs, respectively.

shows the scanning electron microscopy (SEM) image of the TiO_2–UF sample, and the particles are uniform microspheres with diameters around 4.1 μm. Elemental mapping on a randomly picked particle clearly shows a homogeneous distribution of Ti, C, and O across the whole particle (Figure S2), revealing that TiO_2 colloids are evenly encapsulated inside the UF matrix with no preferential position. We also ball mill these particles into broken pieces, and it is obvious that they are solid inside (Figure S3), not surprising for a typical PICA process.[28,29]

After the sample was heated to 500 °C in an argon flow, we observed an obvious shrinkage of the particles while the spherical shapes remained unchanged (Figure 1b). TGA on the sample before heating shows a large loss of the organic species (Figure S4). Interestingly, we find that the particles become hollow in the center, which is not expected for a traditional PICA process.[28] As shown in Figure S5, there exists a large amount of broken shells for the sample being mechanically ground. To have a direct observation on the cross section, we use the technique of FIB to cut the microparticles open. There is no doubt that these particles were indeed hollow, as revealed by the characteristic hole (Figure 1c). The TEM image further confirms the existence of a central cavity, as shown in Figure S6. It notes that our detailed TEM characterization shows that all of the particles are hollow with no exception. Along with the emergence of the cavity, the sample becomes highly crystalline, as revealed by the fingerprint pattern of anatase TiO_2 in its XRD patterns (Figure 1d). For comparison, the original TiO_2–UF sample does not show obvious peaks of TiO_2, probably due to its low crystallinity from a sol–gel process.

As simple as the synthesis might look like, it is intriguing that no previous researchers have paid attention to the possibility of cavity formation from such an old PICA route. We consider that it might be related to two main facts: First, the hollow character is hidden inside the hard thick shell (Figure 1c), and it can be easily overlooked. Second, the product morphology is actually very sensitive to preparation conditions, and good care should be taken if a HHM structure is expected. Typically, the concentrations of TiO_2 sol and UF can have a great effect on the cavity formation. For example, a higher TiO_2 loading of 15 mmol forms solid particles, while a reduced amount of TiO_2 sol produces HHM product as shown in the control test in Figure S7. Further experiments show that the pH value chosen for UF polymerization could also have an effect (Figure S8). From another point of view, the dependence on preparation conditions gives us the ability and necessary flexibility to tune morphologies, such as the shell thickness and cavity size (Figure S9), through systematic control of the reaction details. It also notes that such a synthesis route for the HHM structure is very easy to operate and also economically efficient with full use of cheap industrial raw materials. As shown in Figure S10, it is very convenient for us to prepare 3 g of TiO_2–C HHMs from a one batch synthesis with a TiO_2 yield of 85.6 wt %, which makes it promising for large-scale production.

We find that such a synthesis protocol for HHMs could be readily applied to a large variety of materials such as SnO_2, CeO_2, ZrO_2, and complex metal oxides, as well. Similar to the preparation of TiO_2 HHMs, different MO_x HHMs or MO_x–C HHMs could be easily prepared in a large quantity starting from their inorganic–organic MO_x–UF precursors. Figure 2 shows representative metal oxides, including SnO_2, CeO_2, and ZrO_2, which all exist as highly crystalline microspheres in the final product. Systematic characterizations of the MO_x sol (Figure S11) and MO_x–UF precursors (Figure S12) have been carried out so that the changes of the structure and morphology in the whole process could be well tracked. Similarly, SEM images of the FIB-sectioned specimens confirm that these particles are hollow inside without exception, showing a characteristic HHM structure. In addition to single-component metal oxides, as introduced above, complex material such as multicomponent oxides could also be prepared into uniform microspheres with a good control on size and shape. For example, by using a mixed sol of TiO_2 (4.68 mmol) and SnO_2 (0.56 mmol) for the PICA process, a solid powder of $Ti_xSn_{1-x}O_2$ HHMs was successfully prepared (Figures S13 and S14). Meanwhile, it was also possible to introduce another metal into the system during the heating stage. For example, to prepare a two-component metal oxide of $Li_4Ti_5O_{12}$–C HHMs, a mixture of Li_2CO_3 and TiO_2–UF microspheres was heated

DOI: 10.1021/jacs.6b00773
J. Am. Chem. Soc. 2016, 138, 5916–5922

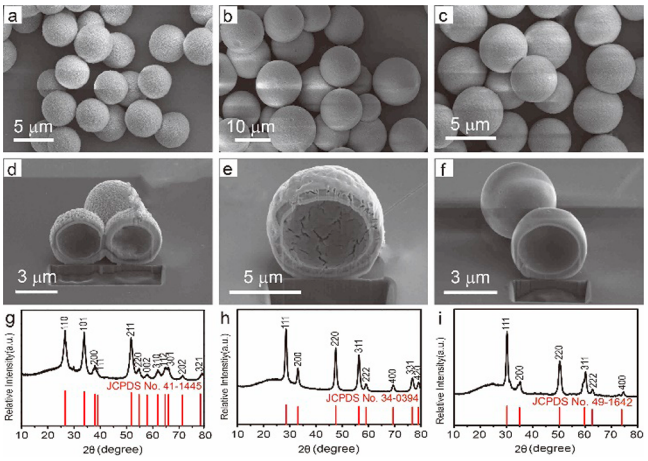

Figure 2. (a–f) SEM images and (g–i) XRD patterns of different MO_x–C HHMs: SnO_2 (a,d,g), CeO_2 (b,e,h), and ZrO_2 (c,f,i). The samples shown in d, e, and f are cut open by FIB sectioning to have a direct observation on the inner cavity.

and a pure phase of $Li_4Ti_5O_{12}$ could be prepared by controlling the amount of Li_2CO_3 and heating conditions (Figure S15).

To have a better understanding on the hollowing process, we carefully characterized the MO_x–UF precursors at different heating stages. Special attention was given to the interior change of the particles with the help of a FIB sectioning technique. Because the MO_x–UF microspheres were gradually heated to a high temperature, we first observed a fast shrinking of the particle size. Typically, the ZrO_2–UF precursor would reduce its size very quickly from 11.6 μm (Figure 3a) to 4.8 μm

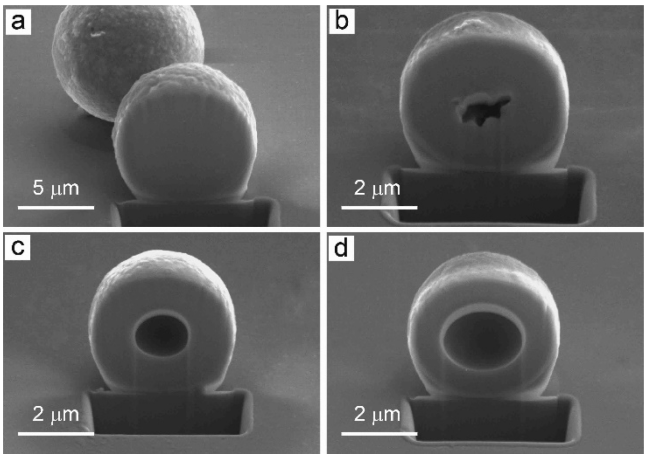

Figure 3. SEM images of the FIB-sectioned ZrO_2–UF samples which have been heated to different temperatures: (a) room temperature (no heating), (b) 350 °C, (c) 450 °C, and (d) 700 °C.

(Figure S16b). At this point, we observed a loss of the majority of UF species (62.9 wt %) according to the TGA results (Figure S16a). Although a large amount of CO_2 was released during heating, the samples had intact shape with no large pores observed inside the particles. XRD characterization (Figure S17) did not show an obvious change, and the sample remained at low crystallinity. As the temperature increased, an irregular tiny crack appeared at around 350 °C in the center (Figure 3b). The crack continued to develop and finally became spherical at 450 °C (Figure 3c). Interestingly, despite the drastic change inside, the particle seemed almost unchanged on the outside and its size remained around 4.8 μm. The following temperature increase resulted in the hollowing out of the center without causing further inward contraction. As the temperature continued to increase to 700 °C (Figure 3d), a typical ZrO_2–C HHM sample formed with a particle size of 4.7 μm and the central cavity around 3.5 μm. Interestingly, for the continuous heating between 450 and 700 °C in the argon flow (Figure S16a), there was no obvious release of CO_2 because only 3.7 wt % weight change was observed; however, an enormous change of the central cavity was observed, indicating that the growth of the cavity was not closely related to the CO_2 release in our synthesis. The XRD patterns recorded at different heating stages show that the sample gradually becomes crystalline (Figure S18).

By using the FIB technique, we were able to precisely section the microspheres into lamellae specimens with a thickness of around 100 nm for TEM examination. In this way, we can have a systematic microarea analysis at different locations inside the particle by exploiting the ability of TEM to determined the structure and chemistry of the materials. With the ZrO_2–C HHM sample as an example, for the above-mentioned particles at different heating stages, we prepared their TEM specimens by sectioning with the FIB lamellae method. Similarly, for the sample heating to 350 °C (Figure 3b), its HRTEM analysis shows that it is almost amorphous and only sporadic nanoparticles can be identified with discernible crystalline lattices (Figure S19), which is in good agreement with its XRD result (Figure S18). As the heating continued, we found that the particle first crystallized on the surface, inducing an obvious difference in the degree of crystallinity along the radial direction. Typically, for the sample heated to 450 °C (Figure 3c), a detailed TEM analysis of its lamellae specimen was carried out to unfold its structural characteristics. To make a stable cut during the FIB sectioning operation, we welded this particle onto the substrate and filled the central cavity by depositing Pt. As expected, the elemental mapping of this slice showed an even distribution of Zr, O, and C (Figure S20), showing a homogeneous mixture of ZrO_2 and carbon. To demonstrate, we selected three representative areas that are located in the radial direction, as labeled in Figure 4a. HRTEM characterization on these three sites clearly showed that they were significantly different in their crystalline state. For site 1, which is the one close to the surface, it is highly crystalline, as revealed by the existence of obvious lattice fringes all over this location (Figure 4b). The fast Fourier transformation (FFT) pattern of its HRTEM image is shown in the inset, and the characteristic FFT points could be well ascribed to the diffraction planes of ZrO_2 (JCPDS No. 49-1642). On the contrary, for the interior territory of site 3, it is mainly amorphous and only tiny and scattered colloids exist (Figure 4c). Accordingly, the FFT analysis does not show obvious diffraction points. For the intermediate zone of site 2, the TEM examination identifies that it is a transition zone, showing a discernible borderline from crystalline to amorphous, as schematically shown by the dashed line in Figure 4d. Further TEM characterization confirmed that this line would go further inside as the temperature increased, leading to a steady expansion of the crystalline area accompanied by the downsizing of the amorphous zone. Finally, the whole particle becomes highly crystalline, and the interior amorphous part totally disappears, forming a typical HHM structure that is highly crystalline all over the particle (Figure S21).

DOI: 10.1021/jacs.6b00773
J. Am. Chem. Soc. 2016, 138, 5916–5922

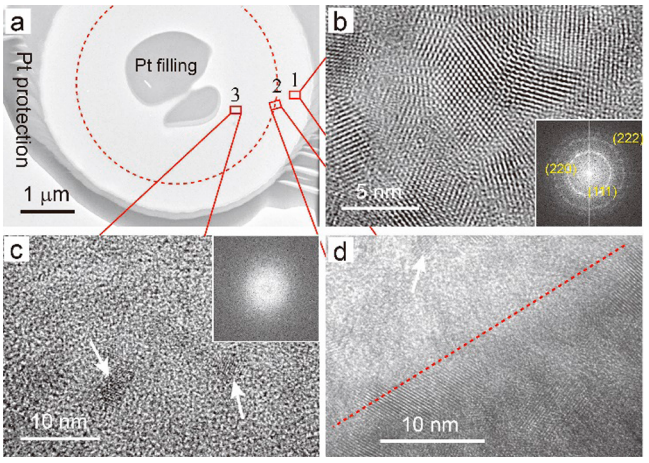

Figure 4. TEM characterization of a ZrO_2−C HHM lamellae sample prepared by the FIB sectioning technique: (a) low-magnification TEM image of the specimen and (b−d) HRTEM analysis for three representative areas in this particle, which are marked in red rectangles. From site 1 to site 3, the sample shows different degrees of crystallinity from highly crystalline to nearly amorphous, and a crystallization boundary can be found in site 2.

The sum of the above observations clearly indicates that formation of HHMs is closely related to their gradual crystallization initiated on the surface. As the frontline of the crystalline layer proceeds inward, the amorphous or less crystalline MO_x colloids will be gradually consumed. Considering the fact that an amorphous phase usually has a much lower density (the tap density of the amorphous TiO_2−C sample is measured to be 1.01 g/cm^3) as compared to its crystalline counterpart (the tap density of the highly crystalline TiO_2−C sample is 1.32 g/cm^3),[30] it is not surprising that such an inward crystallization will gradually proceeded inward, leading to the increase of the tension inside and finally a cleavage of the core. Therefore, the cavity in the center at its earliest stage will exist as cracks with no regular shape, as shown in Figure 3b. During this transition process, two trends, namely, inward crystallization and outward contraction, as illustrated in Scheme 1, occur simultaneously, and the boundary line between crystalline and amorphous regions moves inward until the particles finally become homogeneously crystalline. The continuous movement of a boundary along with the void formation is reminiscent of the Kirkendall effect, in which different interdiffusion rates between a diffusion couple will lead to both the boundary motion and the vacancy enrichment. However, it needs to be pointed out that a traditional Kirkendall effect usually refers to the diffusion of two different kinds of materials rather than two phases.[31] Meanwhile, the transformation of a kinetically unstable amorphous phase into much more stable crystals can also be related to a possible Ostwald ripening effect, which is a thermodynamically driven process with widely discussed dissolution and recrystallization of an unstable phase. Despite the fact that these two different effects have been widely reported and proposed to explain different hollowing phenomena, it is interesting to see that they are usually treated as parallel and unrelated mechanisms proposed for separate cases. For our progressive inward crystallization process, these two effects seem to find a cross point where the diminishment of an unstable phase during a ripening process is achieved by slow diffusion of the crystalline region, showing a characteristic boundary movement of the Kirkendall effect.

Such an efficient method for high-quality HHMs with optimized shell components has significant implications for different applications, such as catalysis, photonics, and energy storage devices. The last of these potentials is demonstrated here by using the anode performance in LIBs as an example. The detailed electrochemical characterizations are shown in Figure 5 for four different samples: LTO-C HHMs, solid LTO-C microspheres, LTO HHMs free of carbon, and solid LTO particles. Despite their differences in composition and shape (see detailed characterization in Figure S22), all of these samples show a pure spinel phase of LTO (Figure S23, JCPDS No. 49-0207). The formation of partially graphitic carbon can be confirmed for the sample heated in an inert atmosphere (Figure S24 for TGA and Raman spectroscopy and Figure S25 for elemental mapping). Figure 5a shows the typical charge/discharge curves of these four different tested samples. Compared to the solid LTO sample, which shows a discharge capacity of 152.9 mAh/g at 0.1 C, the introduction of either a center cavity or a conductive matrix of carbon is able to produce higher discharge capacity, as observed on the sample of LTO HHMs and solid LTO−C microspheres. Not surprisingly, the LTO−C HHMs show the best battery performance among all tests we tried, and it is able to deliver a discharge capacity of 172.8 mAh/g at 0.1 C, which is close to the theoretical capacity of 175 mAh/g. The cyclic voltammogram patterns of the tested samples (Figure S26) revealed the characteristic cathodic and anodic processes during the insertion/extraction of Li^+ in $Li_4Ti_5O_{12}$. Interestingly, we also observed tiny peaks at 1.74 and 1.99 V due to the lithiation/delithiation process of TiO_2,[32,33] whose existence could not been confirmed by our XRD analysis, probably due to its low content and the highly dispersed phase in the LTO−C matrix. The electrochemical impedance spectrum has been known to be a powerful diagnostic tool to probe the electrochemical interface in the cell, and here, we also use this technique to have a better understanding of the kinetics of different samples.[34] Figure 5b shows the Nyquist plots for these four different samples, and

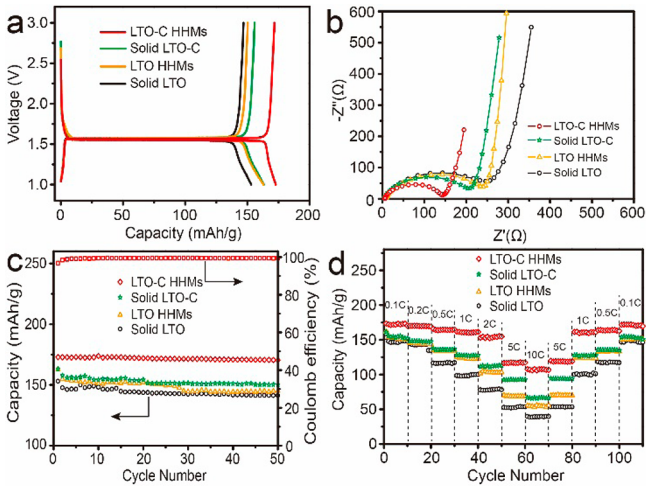

Figure 5. Electrochemical performance for four representative samples as LTO−C HHMs, solid LTO−C, LTO HHMs, and solid LTO: the first charge/discharge curves at 0.1 C (a), EIS spectra (b), cyclability tests at 0.1 C and the Coulombic efficiency for the LTO−C HHM sample (c), and test for different rate capabilities (d).

DOI: 10.1021/jacs.6b00773
J. Am. Chem. Soc. 2016, 138, 5916−5922

the LTO−C HHM sample shows the smallest radius of the semicircle from high-to-medium frequency range, which is known as the charge transfer and surface film resistance (R_{ct}) between electrolyte and active material.[35] Because its R_{ct} of 150 Ω is much lower than that of the other three samples, it is expected that the charge transfer interface reaction occurs more easily for this LTO−C HHM sample, leading to an improved electrochemical performance, as revealed by higher capacity. The advantage of this LTO−C HHM sample for battery applications could be further revealed by the detailed characterizations on cyclability and rate capability tests on different samples. As shown in Figure 5c, LTO−C HHMs show excellent capacity retention over extended cycles. After 50 cycles, the discharge capacity remains at 170.4 mAh/g without obvious fading, and the Coulombic efficiency is constant at around 99.5%. Equally important, the LTO−C HHMs have a much improved rate capability, as shown in Figure 5d. Typically, at a high rate of 10 C, LTO−C HHMs could still give a discharge capacity of 106.8 mAh/g, which is almost 3 times the capacity of a solid LTO sample and shows promising potential for its future application as an anode material in LIBs. We have also tested the full-cell performance by using the high-voltage spinel of $LiMn_{1.5}Ni_{0.5}O_4$ (LMNO) as a cathode material, and the LTO-C HHMs we prepared as the anode. Note that such a LMNO−LTO configuration has been considered to be a promising couple for their application in lithium-ion batteries.[36,37] The data for the battery performance are included in Figure S27. Although the result is only preliminary because it has been a well-known challenge to identify a suitable electrolyte for the high-voltage spinel cathode,[38] we have achieved some promising data for this LMNO−LTO configuration. The discharge capacity was around 107 mA/g at 1 C, and it showed improved cyclability compared to that of the solid LTO samples, further confirming the advantage of the HHMs toward their application as promising electrode materials in lithium-ion batteries.

CONCLUSION

In summary, a synthetic protocol has been developed for the synthesis of hollow hybrid microspheres applicable for different metal oxides. Starting from the preparation of solid inorganic−organic microspheres, we demonstrated that they could become hollow through an interesting process, which we identify as progressive inward crystallization. The solid particles first crystallize on the surface, and then the frontline of the crystallization zone gradually moves inward, leading to the depletion of the core and simultaneous formation of the central cavity. Through such a template-free process, hollow microspheres of different materials including MO_x, MO_x−C, and $M_xM'_{1-x}O$ could be conveniently produced in large quantities. We show that such a synthetic protocol could be very useful for the production of promising anode materials by using LTO as an example. We expect that our findings in these HHMs offer new perspectives in different areas ranging from materials chemistry, energy storage devices, catalysis, and drug delivery.

ASSOCIATED CONTENT

Supporting Information

The Supporting Information is available free of charge on the ACS Publications website at DOI: 10.1021/jacs.6b00773.

Additional experimental details (PDF)

AUTHOR INFORMATION

Corresponding Authors

*anmin_cao@iccas.ac.cn

*wanlijun@iccas.ac.cn

Notes

The authors declare no competing financial interest.

ACKNOWLEDGMENTS

This work was supported by the major State Basic Research Program of China (973 program: 2013CB934000), Strategic Priority Research Program of the Chinese Academy of Sciences (Grant No. XDA09010101), and the National Natural Science Foundation of China (Grant No. 21373238).The authors also thank Prof. Götz Veser from the University of Pittsburgh for his insightful opinions on the hollowing mechanism.

REFERENCES

(1) Caruso, F.; Caruso, R. A.; Möhwald, H. *Science.* **1998**, *282*, 1111.
(2) Lou, X. W.; Archer, L. A.; Yang, Z. C. *Adv. Mater.* **2008**, *20*, 3987.
(3) Tang, S. H.; Huang, X. Q.; Chen, X. L.; Zheng, N. F. *Adv. Funct. Mater.* **2010**, *20*, 2442.
(4) Ha, T. L.; Kim, J. G.; Kim, S. M.; Lee, I. S. *J. Am. Chem. Soc.* **2013**, *135*, 1378.
(5) Yang, Y.; Yang, R. B.; Fan, H. J.; Scholz, R.; Huang, Z. P.; Berger, A.; Qin, Y.; Knez, M.; Gosele, U. *Angew. Chem., Int. Ed.* **2010**, *49*, 1442.
(6) Joo, S. H.; Park, J. Y.; Tsung, C. K.; Yamada, Y.; Yang, P. D.; Somorjai, G. A. *Nat. Mater.* **2009**, *8*, 126.
(7) Lee, I.; Joo, J. B.; Yin, Y. D.; Zaera, F. *Angew. Chem., Int. Ed.* **2011**, *50*, 10208.
(8) Cheng, K.; Peng, S.; Xu, C. J.; Sun, S. H. *J. Am. Chem. Soc.* **2009**, *131*, 10637.
(9) Liu, J.; Qiao, S. Z.; Budi Hartono, S.; Lu, G. Q. *Angew. Chem., Int. Ed.* **2010**, *49*, 4981.
(10) Yu, L.; Wu, H. B.; Lou, X. W. *Adv. Mater.* **2013**, *25*, 2296.
(11) Zhou, X. S.; Yin, Y. X.; Wan, L. J.; Guo, Y. G. *J. Mater. Chem.* **2012**, *22*, 17456.
(12) Liu, N.; Wu, H.; McDowell, M. T.; Yao, Y.; Wang, C. M.; Cui, Y. *Nano Lett.* **2012**, *12*, 3315.
(13) Cong, H. P.; Yu, S. H. *Adv. Funct. Mater.* **2007**, *17*, 1814.
(14) Xu, H. L.; Wang, W. Z. *Angew. Chem., Int. Ed.* **2007**, *46*, 1489.
(15) Dong, Z. H.; Lai, X. Y.; Halpert, J. E.; Yang, N. L.; Yi, L. X.; Zhai, J.; Wang, D.; Tang, Z. Y.; Jiang, L. *Adv. Mater.* **2012**, *24*, 1046.
(16) Dong, Z. H.; Ren, H.; Hessel, C. M.; Wang, J. Y.; Yu, R. B.; Jin, Q.; Yang, M.; Hu, Z. D.; Chen, Y. F.; Tang, Z. Y.; Zhao, H. J.; Wang, D. *Adv. Mater.* **2014**, *26*, 905.
(17) Lai, X. Y.; Li, J.; Korgel, B. A.; Dong, Z. H.; Li, Z. M.; Su, F. B.; Du, J.; Wang, D. *Angew. Chem., Int. Ed.* **2011**, *50*, 2738.
(18) Zhou, L.; Zhao, D. Y.; Lou, X. W. *Adv. Mater.* **2012**, *24*, 745.
(19) Yin, Y. D.; Rioux, R. M.; Erdonmez, C. K.; Hughes, S.; Somorjai, G. A.; Alivisatos, A. P. *Science* **2004**, *304*, 711.
(20) Cao, L.; Chen, D. H.; Caruso, R. A. *Angew. Chem., Int. Ed.* **2013**, *52*, 10986.
(21) Peng, S.; Sun, S. H. *Angew. Chem., Int. Ed.* **2007**, *46*, 4155.
(22) Yi, T. F.; Yang, S. Y.; Xie, Y. *J. Mater. Chem. A* **2015**, *3*, 5750.
(23) Zhu, G. N.; Wang, Y. G.; Xia, Y. Y. *Energy Environ. Sci.* **2012**, *5*, 6652.
(24) Jung, H. G.; Myung, S. T.; Yoon, C. S.; Son, S. B.; Oh, K. H.; Amine, K.; Scrosati, B.; Sun, Y. K. *Energy Environ. Sci.* **2011**, *4*, 1345.
(25) Ma, Y.; Ding, B.; Ji, G.; Lee, J. Y. *ACS Nano* **2013**, *7*, 10870.
(26) Park, K. S.; Benayad, A.; Kang, D. J.; Doo, S. G. *J. Am. Chem. Soc.* **2008**, *130*, 14930.
(27) Wang, Y. Q.; Gu, L.; Guo, Y. G.; Li, H.; He, X. Q.; Tsukimoto, S.; Ikuhara, Y.; Wan, L. J. *J. Am. Chem. Soc.* **2012**, *134*, 7874.
(28) Iler, R. K.; McQueston, H. J. U.S. Patent Appl. US 3855172, 1974.
(29) Jiang, Z. T.; Zuo, Y. M. *Anal. Chem.* **2001**, *73*, 686.

DOI: 10.1021/jacs.6b00773
J. Am. Chem. Soc. 2016, 138, 5916−5922

(30) Li, Y.; Guo, Q.; Kalb, J. A.; Thompson, C. V. *Science* **2008**, *322*, 1816.
(31) Yin, Y. D.; Erdonmez, C.; Aloni, S.; Alivisatos, A. P. *J. Am. Chem. Soc.* **2006**, *128*, 12671.
(32) Rahman, M. M.; Wang, J. Z.; Hassan, M. F.; Wexler, D.; Liu, H. K. *Adv. Energy Mater.* **2011**, *1*, 212.
(33) Liu, H.; Li, W.; Shen, D. K.; Zhao, D. Y.; Wang, G. X. *J. Am. Chem. Soc.* **2015**, *137*, 13161.
(34) Wolfenstine, J.; Lee, U.; Allen, J. L. *J. Power Sources* **2006**, *154*, 287.
(35) Qin, Z. H.; Zhou, X. F.; Xia, Y. G.; Tang, C. L.; Liu, Z. P. *J. Mater. Chem.* **2012**, *22*, 21144.
(36) Li, S. R.; Sinha, N. N.; Chen, C. H.; Xu, K.; Dahn, J. R. *J. Electrochem. Soc.* **2013**, *160*, A2014.
(37) Wu, H. M.; Belharouak, I.; Deng, H.; Abouimrane, A.; Sun, Y. K.; Amine, K. *J. Electrochem. Soc.* **2009**, *156*, A1047.
(38) Julien, C. M.; Mauger, A. *Ionics* **2013**, *19*, 951.

DOI: 10.1021/jacs.6b00773
J. Am. Chem. Soc. 2016, 138, 5916−5922